Iron reduction in profundal sediments of ultra-oligotrophic Lake Tahoe under oxygen-limited conditions

Meret Aeppli[1,2,*], Geoffrey Schladow[3,4], Juan S. Lezama Pacheco[1,5], and Scott Fendorf[1]

[1]*Department of Earth System Science, Stanford University, Stanford, California* 94305*, United States*

[2]*School of Architecture, Civil and Environmental Engineering, EPFL,* 1015 *Lausanne, Switzerland*

[3]*Department of Civil and Environmental Engineering, UC Davis, Davis, California* 95616*, United States*

[4]*UC Davis Tahoe Environmental Research Center, Incline Village, Nevada* 89451*, United States*

[5]*Stanford Synchrotron Radiation Lightsource, SLAC National Accelerator Laboratory, Menlo Park, California* 94025*, United States*

* correspondence: meret.aeppli@epfl.ch

Keywords: lake sediment, iron reduction, nutrient release, anoxia, sediment mineralogy, whole-core incubations

Abstract

Increased periods of bottom water anoxia in deep temperate lakes due to decreasing frequency and depth of water column mixing in a warming climate may result in reductive dissolution of iron minerals and increased flux of nutrients from the sediment into the water column. Here, we assessed the sediment properties and reactivities under depleted oxygen concentrations of Lake Tahoe, a deep ultra-oligotrophic lake in the Sierra Nevada mountain range. Using whole-core incubation experiments, we found that a decrease in dissolved oxygen concentration in the top 2 cm of the sediment resulted in an extension of the microbial iron reduction zone from below 4.5 cm to below 1.5 cm depth. Concentrations of reactive iron generally decreased with sediment depth and microbial iron reduction seemingly ceased as concentrations of Fe(II) approximated concentrations of reactive iron. These findings suggest that microorganisms preferentially utilized reactive iron and/or that iron minerals became less reactive due to mineral transformation and surface passivation. The estimated release of iron mineral-associated phosphorus is not expected to change Lake Tahoe's trophic state, but will likely contribute to increased phytoplankton productivity if mixed into surface waters.

Synopsis

Sediment iron reduction in deep, oligotrophic lakes in a warming climate will increase sediment nutrient fluxes and alter lake ecology and water quality.

Introduction

Climate change causes surface waters in temperate lakes to warm[1], leading to more stable thermal stratification of the water column and, thus, lower frequency and depth of water-column mixing[2–5]. As a consequence, isolated bottom waters are not consistently replenished with oxygen and can experience periods of hypoxia and possibly anoxia[6–8]. Hypolimnetic oxygen depletion causes a shift in organic matter degradation from aerobic to anaerobic pathways[9,10] which can have serious ecological consequences if reduced compounds and nutrients are released from the sediment into the water column[11,12]. Deep, oligotrophic lakes in mountain regions are particularly susceptible to such effects of climate change as these lakes are sensitive to nutrient loading[13] and because climatic warming typically occurs at a faster rate in mountain regions than regions at lower elevation[14].

Lake Tahoe is a deep, ultra-oligotrophic lake in the central Sierra Nevada on the California-Nevada (US) border that serves as an indicator for effects of climate change on oligotrophic lakes worldwide. Annual average surface water temperature of Lake Tahoe has increased mainly as a result of rising air temperatures at an overall rate of 0.21°C per decade[15]. Simulations of lake thermal structure showed that Lake Tahoe will likely cease to mix to the bottom after ~ 2060 in a scenario in which greenhouse gas emissions increase rapidly throughout the 21st Century[2,5]. Should the lake fail to completely mix for more than 6 y in a row, hypolimnetic dissolved oxygen concentration are expected to approach zero[5]. Under such conditions, ferric iron can be used as electron acceptor in anaerobic microbial respiration[16–18]. Given that sediments of Lake Tahoe are rich in iron[12], this respiration pathway is expected to become a a key determinant of biogeochemical conditions

in the hypolimnion as dissolved oxygen concentrations decrease. Ferric iron typically occurs as particulate phase, e.g., in iron oxyhydroxides or ferric iron-containing clay minerals. Reduction of these particulate phases results in the formation of ferrous iron, which can desorb from the particulate surface and be released into the water column where it can stimulate phytoplankton productivity[19–21] or precipitate as iron oxyhydroxide under oxic conditions, forming particles and thereby decreasing water clarity[12,22]. Reductive dissolution of ferric iron minerals can also release adsorbed or co-precipitated phosphorus into sediment porewater and the water column, further alleviating nutrient limitations on phytoplankton productivity[23–25]. Substantial knowledge gaps exist regarding the mineralogy and redox state of iron in the sediments of Lake Tahoe, yet these factors determine if and how fast iron can be microbially reduced[26–29]. Assessing the susceptibility of iron reduction rates to decreasing dissolved oxygen concentrations is key to anticipate consequences of increasing lake temperatures on the release of reduced compounds and nutrients from the sediment.

Here, we study the elemental composition and redox state of profundal sediment of Lake Tahoe as a function of sediment depth and combine these measurements with characterizations of sediment mineralogy by means of X-ray diffractometry and X-ray absorption spectroscopy. To assess changes in iron reduction with sediment depth and shifts in iron reduction as a function of dissolved oxygen concentration, we performed whole-core incubation experiments at three oxygen levels (0.1 %, 5.5 %, and 21 % atmospheric oxygen). We assessed changes in the redox state and reactivity of iron during the incubations.

Materials and Methods

Sediment Sampling. Sediment samples were collected from aboard the UC Davis research vessel R/V John LeConte on September 28, 2020. A box corer (area 0.3 m^2, depth 1.5 m) deployed from the boat was used for sample collection at 449 m depth (42°59′19.1″ N, 108°23′58.6″ W). Samples were collected from a single location as profundal sediment characteristics are fairly homogeneous [12]. On deck, minimally disturbed individual samples were sub-sampled from a single box-core grab into clear acrylic tubes (inner diameter 4.4 cm, 0.32 cm wall thickness) cut at ~ 20 cm or ~ 60 cm length (Tap Plastics). Samples consisted of the top ~ 15 cm or ~ 35 cm of sediment and ~ 5 cm or ~ 20 cm of water, respectively. The tubes were sealed using butyl rubber stoppers and Parafilm. Duplicate cores for in-situ sediment characterization were frozen ~ 2 h after collection, cut into 1.5 cm wide slices and sealed into Mylar bags with oxygen scrubbers, and stored at -20°C until analysis. Cores for the incubation experiments were stored upright at 4 - 10°C until being used in the experiments.

Whole-Core Incubation Experiments. Cores were incubated in air-tight half gallon glass jars at 5°C at three atmospheric oxygen levels of 0.1 %, 5.5 %, and 21 % for 74 d (see Figure S6 for photos of the cores). Prior to incubation, cores were pre-incubated for 11 weeks at 10°C to ensure that monitored processes were not an artefact of sampling. For each treatment, duplicate cores were prepared by adapting the water level above the sediment-water interface to 2 cm height. Glass jars were flushed with pure nitrogen (0.1 % atmospheric oxygen), a mix of nitrogen and compressed air (5.5 % atmospheric oxygen, gases were mixed using a Cole-Parmer Masterflex Variable-Area Flowtube), or compressed air (21 % atmospheric oxygen). The oxygen concentration in the jars was

checked after flushing and before each sampling timepoint using optical oxygen sensor spots and an oxygen meter (PreSens). Measured values remained within 0.1 - 0.2 % for the 0.1 % atmospheric oxygen treatment, 5.5 - 5.7 % for the 5.5 % atmospheric oxygen treatment, and at 21 % for the 21 % atmospheric oxygen treatment throughout the experiment. At selected time points during the experiment (i.e., at 3 d, 8 d, 15 d, 37 d, 57 d, and 74 d), dissolved oxygen profiles were measured in the cores using an oxygen microsensor mounted on a motor stand (UniSense). Profiles were recorded within 5 minutes of opening the glass jars from 1 cm above the sediment-water interface to 3.5 cm sediment depth at 1 mm intervals. pH was measured directly in the water overlaying the sediments in each core (Figure S10). In addition, sediment and water aliquots (0.25 mL aliquots from 0.5 cm above the sediment-water interface, and from 0.5 cm, 1.5 cm, 3 cm, 4.5 cm, 6.0 cm, and 7.5 cm sediment depth) were collected from the cores using a cut-off syringe and in a clockwise fashion as the experiment progressed (illustration in Figure S5). Samples from duplicate cores were pooled without any further treatment and suspended into deoxygenated, deionized water (0.5 mL sample into 4.5 mL deoxygenated, deionized water). The diluted samples were used in aqueous and solid phase analyses as described below. Sediment and water sampling was performed under constant nitrogen flow to avoid oxidation of ferrous iron and sulfide in the sample aliquots. Glass jars containing cores were re-sealed after sampling and flushed as described above.

Aqueous Phase Analysis. Diluted sediment and water samples collected during the incubation experiments were filtered (0.22 μm polyethersulfone (PES)) for aqueous phase analysis. Dissolved sulfide levels were determined on freshly collected and filtered samples using the N,N−dimethyl−p−phenylenediamine method[30]. No sulfide was detected in any of the samples. Dissolved

ferrous iron concentrations were determined after extraction of unfiltered samples in 0.5 M HCl for 1 h followed by filtration (0.22 μm PES) using the ferrozine method[31]. Colorimetric measurements for sulfide and ferrous iron were performed on a microplate reader (Synergy 2, BioTek).

Solid Phase Analysis and Chemical Extractions. Cores that were frozen after collection (referred to as in-situ cores, see above) were used for solid phase analysis. Frozen core slices of 1.5 cm width were thawed and dried in an anoxic glovebag and subsequently finely ground with mortar and pestle. Total elemental composition of the samples was determined using X-ray fluorescence spectroscopy (Spectro Xepos HE XRF Spectrometer) and, in the case of C and N, elemental analysis (NA1500, Carlo Erba Elemental Analyzer).

Chemical extractions were performed on sediments collected from in-situ cores and from the incubated cores at the endpoint of the experiment in 1.5 cm intervals. Samples were extracted in deionized water (2 mL sample per 10 mL) and hydrochloric acid 0.5 M (2 mL sample per 5 mL) in 15 mL Falcon tubes. The sample suspensions were shaken for 2 h and centrifuged (3000 rpm; 15 min). The supernatant was then decanted and filtered (0.22 μm PES). Aqueous concentrations of Mn were determined on water extracts using an ICP optical emission spectrometer (ICAP 6300 Duo View, Thermo). Concentrations of ferrous and total iron were determined on the acid extracts using the ferrozine method (see above) and hydroxylamine as reducing agent[32].

Mediated Electrochemical Measurements. Diluted sediment samples collected during the incubation experiments under nitrogen flow were immediately frozen at -20°C for mediated electrochemical measurements to avoid changes in the redox state of iron during sample collection.

Mediated electrochemical reduction (MER) and oxidation (MEO) were used to determine the electron accepting (EAC) and donating capacity (EDC) of the samples. The electrochemical setup consisted of an eight-channel potentiostat (model 1000C, CHInstrument, US) and eight electrochemical cells. Each cell consisted of a glassy carbon working electrode cylinder, which served as reaction vessel (9 mL, GAZ 1 HTW), a platinum wire as counter electrode and separated from the working electrode compartment by a glass frit (PORE E tubes, ACE glass), and an Ag/AgCl reference electrode (Re1B, ALS). Reduction potentials are reported versus the standard hydrogen electrode herein.

Electrochemical measurements were performed in pH-buffered solutions at pH 5.0 (0.01 M acetate and 0.01 M KCl, 5 mL per electrochemical cell) and at applied reduction potentials for $E_{\mathrm{H}}^{\mathrm{MER}} = -0.57$ V in MER cells and $E_{\mathrm{H}}^{\mathrm{MEO}} = +0.82$ V in MEO cells. Under these conditions, we expect all ferric iron in oxy(hydr)oxides[33] and clay minerals[34] as well as oxidized quinone groups in organic matter[35] to be reduced in MER, and all ferrous iron[26], sulfide[36], and reduced quinone groups in organic matter[35] to be oxidized in MEO. Measurements were performed using the electron electron transfer mediators paraquat (1,1′-dimethyl−4,4′-bipyridinium, standard reduction potential E_{H}^{0}=−0.46 V[37]) in MER and ABTS (2,2′-azino-bis(3-ethylbenzothiazoline-6-sulfonic acid), E_{H}^{0}=+0.70 V[38]) in MEO. These mediators were added to the electrochemical cells and equilibrated to the applied potentials prior to sample additions (final concentrations of reduced paraquat in the MER and oxidized ABTS in the MEO cells: 0.28 mM). For electrochemical measurements, the diluted sediment samples collected during the incubation experiments were further diluted by adding 100 μL sample suspension to 300 μL deionised water. Of these latter supensions, we added 20 μL to each MER and MEO cell. Measurements were stopped at most 1 h after sample addition when

currents had returned to baseline values that were measured before sample additions.

EAC and EDC of the samples (in mol electrons transferred per g of dry sample) were determined by integration of reductive and oxidative current peaks, respectively, that resulted from sample additions to the electrochemical cells according to eqs. 1 and 2.

$$\mathrm{EAC} = \frac{1}{F \cdot \mathrm{DW}} \cdot \int_{t_0}^{t_{end}} I_{red}\, \mathrm{d}t \tag{1}$$

$$\mathrm{EDC} = \frac{1}{F \cdot \mathrm{DW}} \cdot \int_{t_0}^{t_{end}} -I_{ox}\, \mathrm{d}t \tag{2}$$

where I_{red} and I_{ox} are the baseline-corrected reductive and oxidative currents, respectively (A), F is the Faraday constant, DW is the dry weight of the sample in g, and t_0 and t_{end} (s) are the initial and final integration boundaries for each current peak. The electron exchanging capacity (EEC, in mol electrons transferred per g of dry sample) is the sum of EAC and EDC.

X-ray diffractometry. X-ray diffractograms were recorded (MiniFlex 600, Rigaku) from 3 to 90° 2Θ (step size 0.02° 2Θ) in Bragg-Brentano geometry using Cu Kα radiation (40 kV and 40 mA) and a silicon strip detector (D/teX Ultra) or a 2D hybrid pixel array detector (HyPix-400 MF). The identities of sediment components were determined using the SmartLab Studio-II software and published structure files for quartz (ICSD code 01-086-1629), and members of the feldspar group (sodium aluminum silicate (00-010-0033), sodium calcium aluminum silicate (01-079-1149), and

potassium aluminum silicate (00-019-0931)).

X-ray absorption spectroscopy. Extended X-ray Absorption Fine Structure (EXAFS) Fe K-edge spectra were collected at beamline 7-3 at the Stanford Synchrotron Radiation Lightsource (SSRL). Samples were prepared inside an anoxic chamber by pressing finely ground sample material into Al holders and covering them with Kapton tape. The Al holders were stored in an air-tight jar under anoxic atmosphere before being rapidly transferred into the liquid He cryostat for analysis. The Si(220) double crystal monochromator was calibrated by setting the first inflection point of the absorption K-edge of a Fe metal foil to 7500 eV. For each sample, 3 scans were recorded in transmission mode using a Lytle detector. Spectra were processed and analyzed using the Demeter software package[39]. Linear combination-least squares fitting was performed using reference spectra for ferrihydrite[40], ferrosmectite, nontronite[41], biotite[42], and hornblende (Figure S3 and Table S2).

Results and Discussion

Sediment profile. Figure 1a shows a photo of the top 10 cm of a sediment core. The top ~ 1 cm of sediment consisted of suspended material that moved with the overlaying water, whereas material below was more consolidated; consistent with these observations, sediment density increased from around 0.173 ± 0.08 g cm^{-3} at 0.5 cm to 0.262 ± 0.07 g cm^{-3} at 7.5 cm (Table S1). We determined the elemental composition of the sediment on sediment cores that were frozen after collection. Manganese (Mn) and iron (Fe) concentrations peaked at 0.21 mmol g^{-1} at 3 - 4.5 cm and 1.54 mmol g^{-1} at 4.5 - 6 cm, respectively (Figure 1b, c; corresponding weight percentages in Figure S1a, b). To

assess variations in the redox state of Mn and Fe as well as other solid phase electron acceptors with depth, we quantified total electron accepting capacity (EAC) and electron donating capacity (EDC) of sediment samples using mediated electrochemistry. EAC reflected the response of particulate phases containing oxidized Mn or Fe[33,34,36] and quinone groups in dissolved and particulate organic matter[35] to strongly reducing conditions in electrochemical cells; EDC reflected the response of dissolved and solid-associated reduced Mn and Fe species and hydroquinone groups in dissolved and particulate organic matter[35] to strongly oxidizing conditions in electrochemical cells. The dissolved electron acceptors oxygen, nitrate, and sulfate are not electro-active in electrochemical cells and therefore do not contribute to EAC nor EDC[36]. We note that dissolved sulfide, which produces an electrochemical response under oxidizing conditions[36], was not detected in any of the sediment samples. Figure 1g shows that EAC/EEC decreased from fully oxidized (EAC/EEC = 0.99 ± 0.01) at 0 - 3 cm to partially reduced (EAC/EEC = 0.75 ± 0.14) at 6 - 7.5 cm. Consistent with this decrease, the concentration of dissolved species contributing to EDC increased: the concentration of water-extractable Mn (which we assume to be Mn^{2+} under experimental conditions) increased with depth below 3 cm (Figure S7d) and the concentration of acid-extractable Fe(II) increased with depth below 4.5 cm (Figure 4a-c). Interpreted alongside the Mn and Fe concentration profiles in Figure 1b, c, these data indicate that microbial reductive dissolution of Mn oxyhydroxides was an important respiration pathway at 3 - 6 cm depth, while reductive dissolution of Fe oxyhydroxides was dominant below 4.5 cm depth. This interpretation was also consistent with the change in color from brown-black (the color of Mn and Fe oxyhydroxides) to grey in the top 10 cm of the sediment (Figure 1a). In the top ~ 1.5 cm, nitrate and oxygen were likely the dominant electron acceptors,

193 as indicated by elevated nitrate concentrations of 0.08 μm g^{-1} compared to < 0.04 μm g^{-1} below
194 1.5 cm (Figure 1f) and a rapid decrease in dissolved oxygen concentrations from 0 to 1.5 cm, as
195 discussed below (Figure 3).

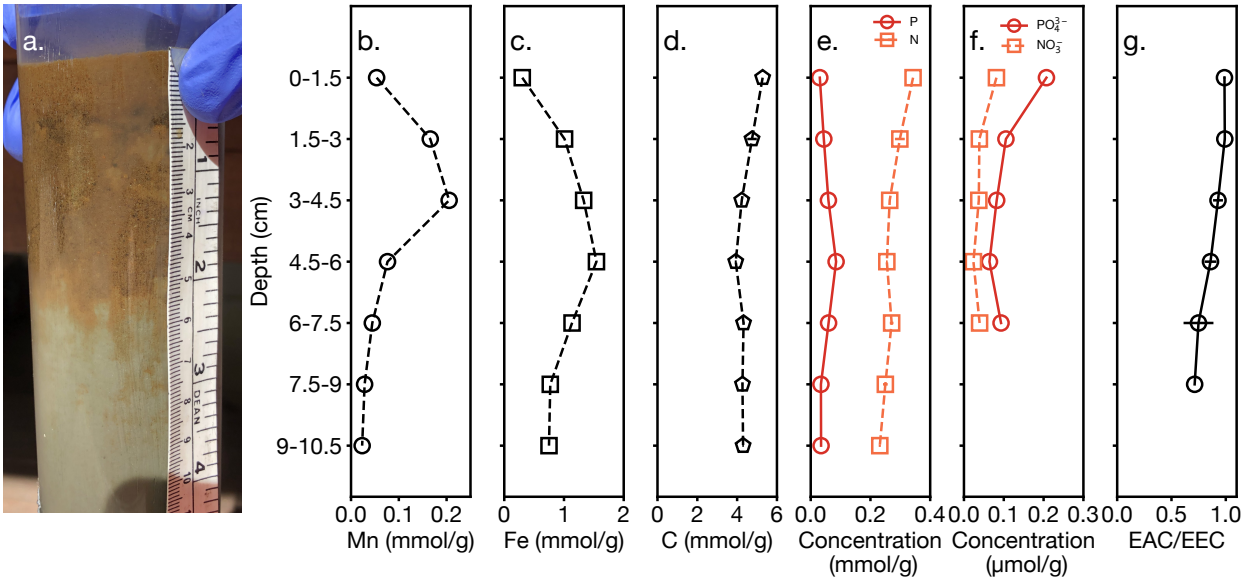

Figure 1. Sediment profile. **a.** Photo of a sediment core and corresponding concentrations of **b.** total manganese, **c.** total iron, **d.** total carbon, **e.** total phosphorus and nitrogen, and **f.** dissolved phosphate and nitrate. **g.** Redox state of sediment expressed as ratio of electron accepting capacity (EAC) to total electron exchanging capacity (EEC, equals sum of EAC and electron donating capacity). Errorbars in panels d-f represent duplicate measurements on single samples. Figure S2 shows the data in panels b-e as weight percentages and molar ratios of C:N and Fe:P with depth. Analyses were performed on sediment cores that were frozen after collection to represent in-situ conditions in the lake.

196 Total carbon (C) concentrations showed the inverse trend to Fe concentrations at 0 - 6 cm,
197 and stabilized at 4.3 ± 0.04 mmol g^{-1} below 6 cm (Figure 1d; corresponding weight percentages in

Figure S1c). Concentration profiles of total nitrogen (N) mirrored those of total C (Figure 1e) and the C:N molar ratio of 15.7 ± 1.7 did not change systematically with depth (Figure S1e). Based on these C:N ratios, organic matter in the sediments primarily originated from land-derived organic matter which has C:N ratios higher than 14 - 20, rather than C:N ratios of 4-10 associated with phytoplankton and aquatic macrophytes[43]. Total phosphorus (P) concentrations peaked at 0.08 mmol g^{-1} at 4.5 - 6 cm (Figure 1e), paralleling total Fe concentrations (Figure S2). Conversely, dissolved phosphate decreased with increasing depth in the top few cm (Figure 1f). These trends suggest that P entered the sediment from the water column as dissolved phase and partitioned into the solid phase a few cm into the sediment through the association with Fe phases. The molar ratio of Fe:P was 9.9 at 0 - 1.5 cm (and increased to values above 20 at 3 - 10.5 cm, Figure S1e), which was consistent with previous P:Fe ratios for Lake Tahoe sediments[12] and with P being primarily associated with Fe oxyhydroxides[23–25].

X-ray diffraction and EXAFS analyses showed that Fe occurred primarily in the form of Fe oxyhydroxide and Fe-containing phyllosilicate clays. Figure 2 shows an exemplary X-ray diffractogram and EXAFS spectrum collected on the 1.5 - 3 cm sample as representative example for Fe mineralogy in the top 7.5 cm of the sediment (see Figures S3 and S4 for other samples). Across 0 - 7.5 cm depth, the amorphous Fe oxyhydroxide mineral ferrihydrite accounted for 32-44% of Fe in the samples according to EXAFS analysis (Figure 2b and Table S2). The majority (56-68 %) of Fe occurred in the form of Fe-containing phyllosilicate minerals based on EXAFS analysis. In addition to these Fe-containing minerals, X-ray diffractograms showed characteristic peaks for quartz and aluminumsilicates with various elemental composition, including members of the plagioclase

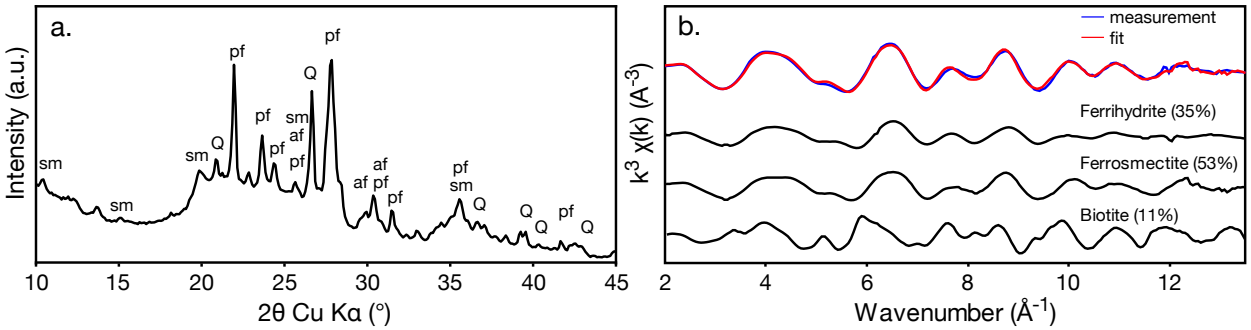

Figure 2. Mineralogy of exemplary sediment sample collected at 1.5 - 3 cm depth. **a.** Representative X-ray diffractogram with characteristic peaks for quartz (Q), and members of the plagioclase feldspar (pf), alkali feldspar (af) and smectite (sm) groups. **b.** Fourier transforms of bulk Fe K-edge EXAFS spectrum (blue line) and linear combination-least squares fit (red line; fitted values are shown on the right). References used in the fit are shown in black (ferrihydrite, a Fe oxyhydroxide; ferrosmectite and biotite, two Fe-containing phyollosilicate minerals). Results for samples collected at other depths are shown in Figures S3 and S4, and Table S2.

feldspar group (containing Na and/or Ca) and alkali feldspar groups (containing K; see Figure S2a, b for Ca, Na, K, and Al concentration profiles).

Influence of dissolved oxygen concentration on sediment profiles. To assess the effect of decreased dissolved oxygen concentration on sediment redox processes, we incubated whole sediment cores under three atmospheric oxygen levels (setup in Figure S5). We used treatments with 0.1 % and 21 % atmospheric oxygen as reference points for anoxic and oxic systems, respectively. In addition, we used an intermediate atmospheric oxygen concentration of 5.5 % to mimic incomplete depletion of dissolved oxygen.

Figure 3a-c shows dissolved oxygen profiles recorded at selected time points throughout the incubation experiments. Initial profiles (light green) at the start of the experiments were similar for all treatments. Within the first 3 d, dissolved oxygen concentration at the sediment-water interface decreased to concentrations in the overlaying water in the 0.1 % and 5.5 % atmospheric oxygen treatments. Thereafter, concentration profiles remained constant over the course of the 74 d experiment. The 21 % atmospheric oxygen treatment showed no systematic changes in profiles throughout the experiment. In the 5.5 % and 21 % atmospheric oxygen treatments, measured concentrations of dissolved oxygen in the water overlying the sediments were lower than calculated equilibrium concentrations of 82 μmol L^{-1} for 5 % treatment and 400 μmol L^{-1} for 21 % treatment at 5°C, presumably due to microbial oxygen consumption in the water column. Dissolved oxygen concentrations decreased rapidly into the sediments in these treatments due to microbial consumption. No dissolved oxygen was detected below 1.5 cm in any of the treatments. The depth of oxygen penetration differed slightly between the cores, which was likely due to differences in the distribution of sediment layers along depth: in cores incubated under 0.1 % and 5.5 % atmospheric oxygen, the layer of unconsolidated material at the sediment-water interface extended further down than in cores incubated under 21 % atmospheric oxygen (see photos in Figure S6), consistent with lower sediment density values for the former two (Table S1). We note that under in-situ conditions in the lake, we would expect dissolved oxygen to penetrate deeper into the sediment than in our experimental setup due to advective movement. This expectation is consistent with the in-situ EAC/EEC and nitrate concentration profiles in Figure 1d, g, which indicate that aerobic and nitrate respiration were the dominant microbial respiration pathways at 0 - 3 cm depth.

We assessed how the redox state of the sediment changed as a consequence of changes in dissolved oxygen concentrations and associated shifts in microbial respiration pathways. Figure 3d-f shows EAC/EEC values of sediment samples collected from 0.5 cm, 1.5 cm, and 3 cm depth at selected time points during the incubation experiments. An EAC/EEC value of 1 indicates a fully oxidized sample, whereas a value of 0 indicates a fully reduced sample. In all treatments, EAC/EEC decreased at 3 cm depth over the course of the experiments due to the buildup of EDC. The buildup corresponded to the formation of acid-extractable Fe(II) (Figure S9). This finding suggests that microbial Fe(III) reduction was the dominant pathway for microbial respiration, which was consistent with the absence of dissolved oxygen at this depth. The decrease in EAC/EEC at 0.5 cm was more pronounced in the 0.1 % atmospheric oxygen treatment than in the other two treatments, presumably because oxygen was not available in the former treatment and hence Fe(III) was the most thermodynamically favorable electron acceptor for microbial respiration. Accordingly, Fe(II) formation rates calculated from the EDC data at 0.5 cm depth were higher in the 0.1 % atmospheric oxygen treatment with 0.6 μmol g^{-1} d^{-1} compared to 0.1 μmol g^{-1} d^{-1} and 0.2 μmol g^{-1} d^{-1} in the 5.5 % and 21 % atmospheric oxygen treatments, respectively. In agreement with similar redox conditions across all cores below 1.5 cm depth, Fe(II) formation rates were similar for all treatments at 3 cm depth, with 1.3 μmol g^{-1} d^{-1} for the 0.1 %, 1.0 μmol g^{-1} d^{-1} for the 5.5 %, and 1.3 μmol g^{-1} d^{-1} for the 21 % atmospheric oxygen treatment.

Iron reduction dynamics. We extended our analysis of changes in sediment redox state beyond 3 cm to 7.5 cm depth. Figure 4a-c compares profiles of acid-extractable Fe(II) at the onset of the experiment (quantified on sediments immediately frozen after collection, filled symbols) to profiles

of acid-extractable Fe(II) at the endpoint of the experiments after 74 d (quantified on treatment cores, empty symbols). Profiles were similar across all treatments below 1.5 cm depth, consistent with the absence of dissolved oxygen (Figure 3a-c). Elevated concentrations of acid-extractable Fe(II) were observed in the 0-1.5 cm depth interval for the 0.1 % atmospheric oxygen treatment. The concentration of acid-extractable Fe(II) matched EDC within errors in all treatments (Figure S9). Given that EDC represents the cumulative response of both dissolved and solid-phase associated reduced redox-active species, this suggests that Fe(II) was either dissolved or adsorbed to particulate surfaces, or occurred as an easily extractable solid phase. The zone of microbial Fe reduction extended from 0 - 1.5 cm (0.1 % atmospheric oxygen treatment) or 1.5 cm (remaining treatments) to 6 - 7.5 cm depth based on the increase in acid-extractable Fe(II) in this zone. Compared to the in-situ conditions in Figure 1g, the upper end of the Fe reduction zone in our incubation experiments therefore extended upwards from 4.5 cm to at least 1.5 cm (see Figure S11 for changes in EAC/EEC in the treatments). Therefore, the lack of oxygen in the top few cm of the sediment stimulated microbial Fe reduction in layers closer to the sediment-water interface.

Within the zone of microbial Fe reduction, we observed differences in the reactivity of Fe phases. The concentration of acid-extractable total Fe, i.e., the sum of acid-extractable Fe(II) and hydroxylamine-reducible Fe(III), was decreased at 3 - 6 cm depth in all treatments relative to the initial concentration profiles (Figure 4a-c). These trends indicate that Fe minerals became harder to reduce over the course of the incubations given that hydroxylamine-reducible Fe serves as proxy for microbially reducible iron[32]. A possible explanation for this observation is the preferential use of easily reducible Fe minerals by iron-reducing microorganisms[22,44,45]. It is also possible

that elevated Fe(II) concentrations at 3 - 6 cm depth caused transformation of ferrihydrite into less reactive phases or resulted in passivation of mineral surfaces[46]. The in-situ core showed the same trends of decreased acid-extractable total Fe concentrations below 4.5 cm (Figure 4a-c, filled symbols), suggesting that similar processes as those observed in our experiment were taking place under in-situ conditions in these lower layers at 4.5 - 7.5 cm.

Panels d-f in Figure 4 show the same data as panels a-c but expressed as percentage of total sediment Fe. In the top 1.5 cm, around 65 % of total Fe was reactive; this fraction decreases to around 10 % in the lowest layer for both the initial material and the endpoint material. The higher reactivity of Fe minerals closer to the sediment-water interface potentially results from the sedimentation of recently precipitated, highly amorphous iron oxide particles[22,47]. In the anoxic parts of both the experimental and in-situ cores, microbial Fe reduction proceeded until 5 - 10 % of Fe had been reduced. This finding suggests that the fraction of microbially reducible Fe was similar across the entire zone of Fe reduction. Given that Fe reduction in our experimental cores was not more extensive in the in-situ core at depths below 4.5 cm, we consider it likely that microbial Fe reduction would not proceed beyond 10% of total sediment Fe even for longer incubation times. This is consistent with an observed cessation of Fe(II) production toward the end of our incubations (Figure S9).

Implications. Our work shows that microbial Fe reduction in Lake Tahoe sediment currently occurs primarily at and below 4.5 cm depth. The upper limit of the Fe reduction zone significantly extended to 1.5 cm depth when the dissolved oxygen concentration at the sediment-water interface was reduced

to zero in our experiments. Hypolimnetic dissolved oxygen concentrations are projected to decrease in response to decreased depth and frequency of lake mixing in the following decades[2,5] and this decrease will likely cause the sediment Fe reduction zone to extend toward the sediment-water interface. Our results suggest that microbial Fe reduction will proceed until around 10% of total sediment Fe is reduced and that this value is determined by the amount of reactive Fe phases and Fe(II) accumulation. Fe(II) produced in the sediment may be released into the water column where it would be rapidly oxidized and precipitate as iron oxyhydroxides upon contact with oxygen[12,22]. While we consider it unlikely that Fe(II) is mixed into surface waters and induces algal blooms, the release of phosphorus during reductive dissolution of sediment iron minerals poses a bigger threat to lake ecology[23–25]. If we assume that 10 % of Fe in the top 1.5 cm of sediment are reductively dissolved and phosphorus was homogenously mixed into the entire lake water body, phosphorus concentrations in the water column would increase by around 1.2 μg L^{-1} (using a total lake volume of 152 km^3 [12],) in line with previous findings by Beutel and Horne[12]. While this amount would not change the trophic status of Lake Tahoe, Beutel and Horne[12] suggested that it would result in a 40 % increase of phytoplankton productivity. Therefore, there is a need for continuous monitoring of oxygen saturation in lake bottom waters for early detection of internal nutrient loading in oligotrophic lakes.

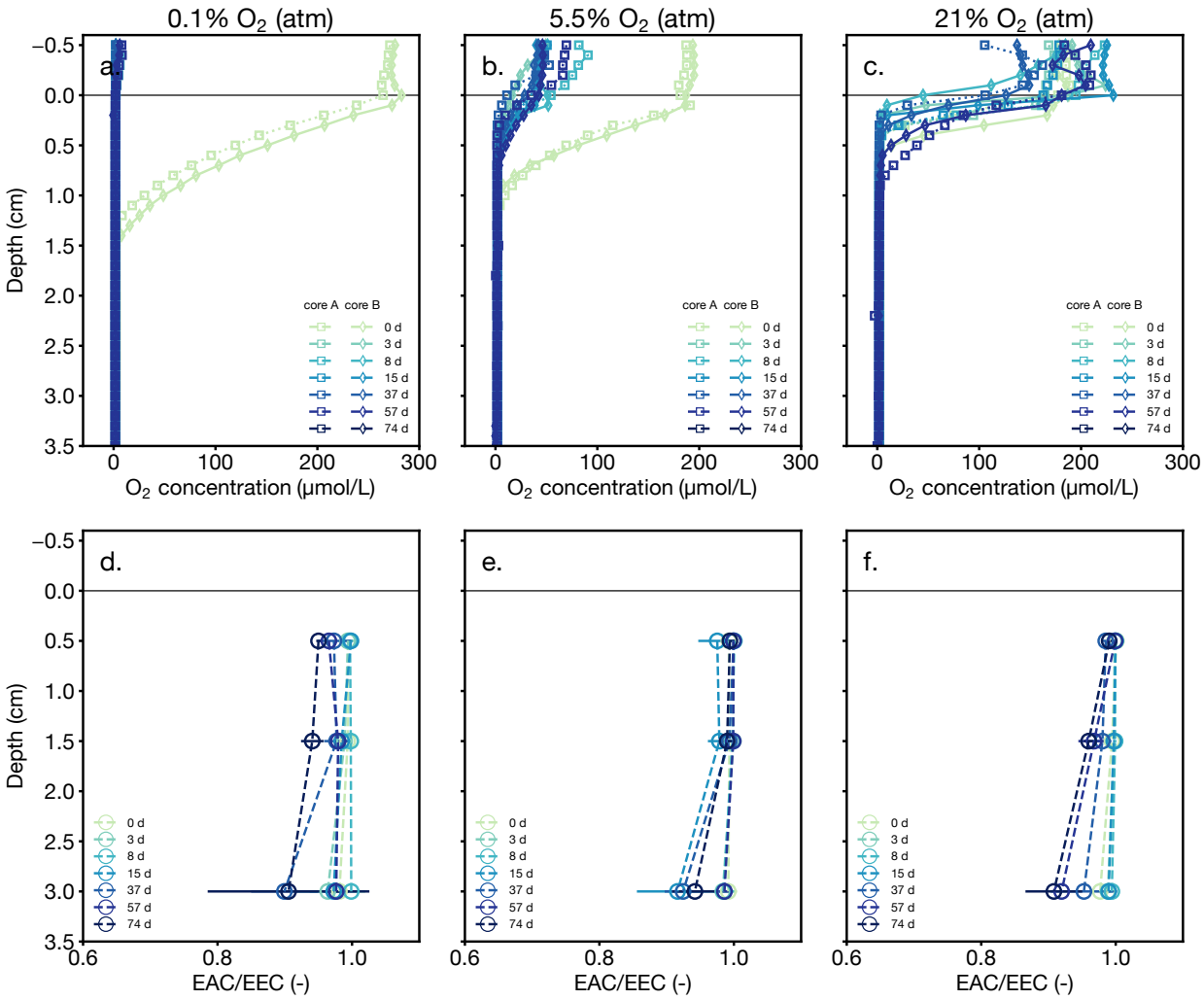

Figure 3. Dissolved oxygen and sediment redox profiles in whole-core incubation experiments under 0.1 %, 5.5 %, and 21 % atmospheric oxygen. **a.-c.** Dissolved oxygen profiles collected at selected time points during the incubation experiments from 0.5 cm above the sediment-water interface at 0 cm down to 3.5 cm sediment depth at 1 mm intervals. Results are shown separately for the duplicate cores in each treatment. **d.-f.** Corresponding changes in the ratio of electron accepting capacity (EAC) to electron exchanging capacity (EEC, sum of EAC and electron donating capacity) of sediment samples collected at 0.5 cm, 1.5 cm, and 3 cm depth at selected time points during the incubation experiments. Error bars represent mean absolute deviations of duplicate measurements on each pooled sediment sample.

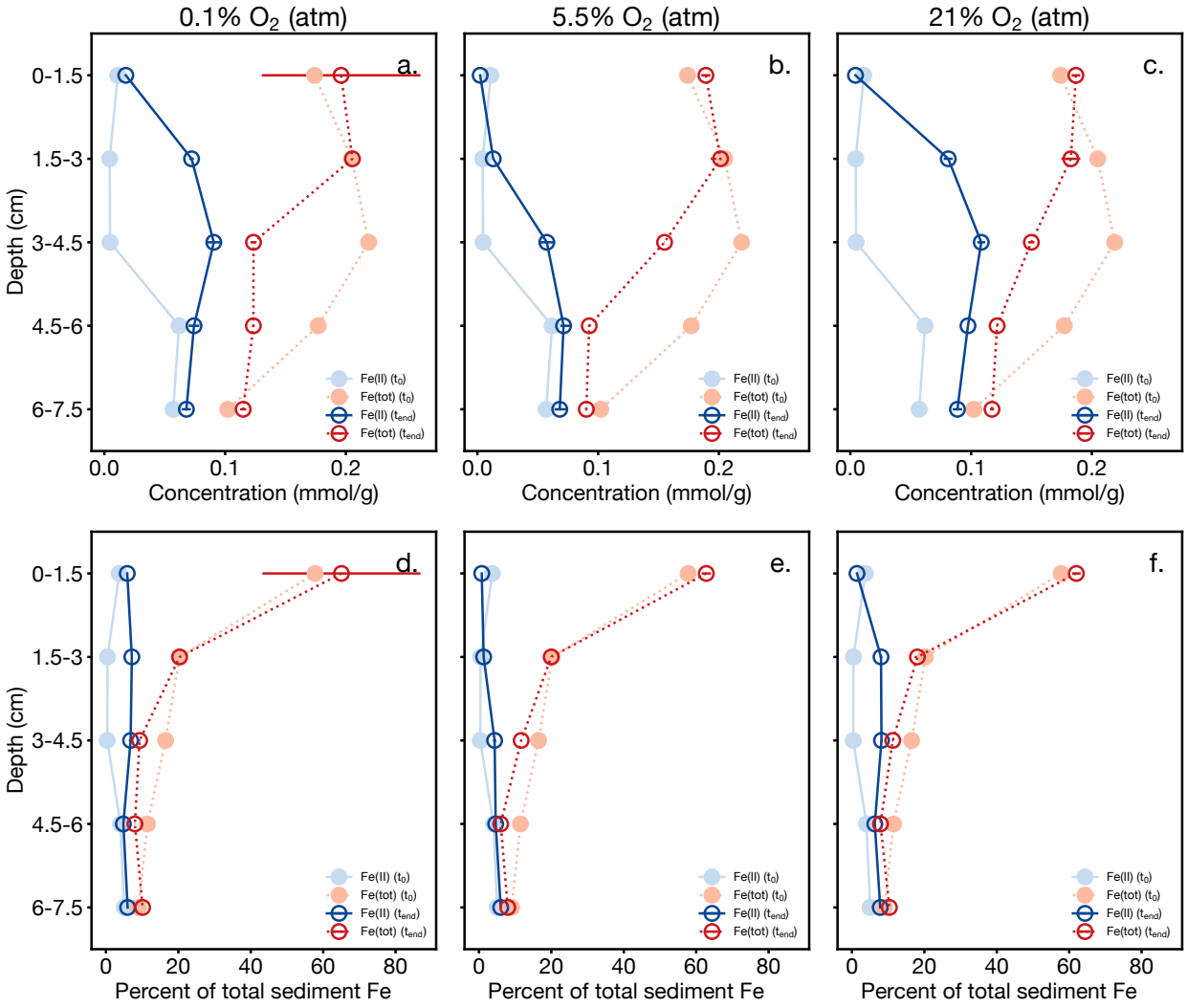

Figure 4. Fe(II) production dynamics in whole-core incubation experiments under 0.1 %, 5.5 %, and 21 % atmospheric oxygen. **a.-c.** Profile of acid-extractable Fe(II) and acid-extractable total Fe (Fe(tot), sum of acid-extractable Fe(II) and hydroxylamide-reducible Fe(III)) for the start (t_0, filled symbols, quantified on cores frozen upon collection) and the end (t_{end}, empty symbols, quantified on experimental cores at the end of incubation experiments) of the experiments. **d.-f.** Profiles of acid-extractable Fe(II) and acid-extractable Fe(tot) expressed as percentage of total sediment Fe. Error bars represent mean absolute deviations of duplicate measurements on each pooled sediment sample.

Acknowledgements and Funding Sources

The authors thank Dr. Guangchao Li, and Douglas Turner for analytical and technical support. Furthermore, the authors thank Brant Allen, the captain of R/V John Le Conte, and Nancy Hardesty, who generously made her house available. Financial support for Aeppli was provided through a postdoctoral fellowship by the Swiss National Science Foundation (project number P2EZP2_188076).

Supporting Information Available

Sediment elemental composition and density, Fe K-edge EXAFS spectra and fitting results, X-ray diffractograms, schematic of experimental setup, photos of experimental cores, depth profiles for concentrations of Fe(II), total Fe, and water-extractable Mn, temporal changes in electron donating capacity and HCl-extractable Fe(II) during incubation experiments, depth profiles for electron accepting capacity.

Graphical TOC entry

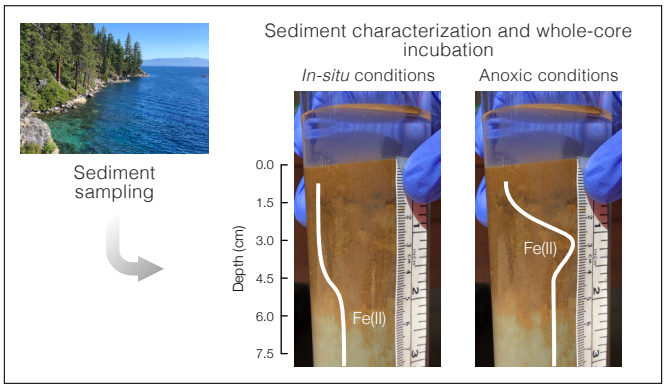

References

1. Bates, B., Kundzewicz, Z., Wu, S., and Palutikof, J. *Technical Paper of the Intergovernmental Panel on Climate Change*; IPCC Secretariat: Geneva, 2008; p 210.

2. Sahoo, G. B., Forrest, A. L., Schladow, S. G., Reuter, J. E., Coats, R., and Dettinger, M. (2016) Climate change impacts on lake thermal dynamics and ecosystem vulnerabilities. *Limnol. Oceanogr. 61*, 496 – 507.

3. Butcher, J. B., Nover, D., Johnson, T. E., and Clark, C. M. (2015) Sensitivity of lake thermal and mixing dynamics to climate change. *Clim. Change 129*, 295–305.

4. Schwefel, R., Gaudard, A., Wüest, A., and Bouffard, D. (2016) Effects of climate change on deepwater oxygen and winter mixing in a deep lake (Lake Geneva): Comparing observational findings and modeling. *Water Resour. Res. 52*, 8811–8826.

5. Sahoo, G. B., Schladow, S. G., Reuter, J. E., Coats, R., Dettinger, M., Riverson, J., Wolfe, B., and Costa-Cabral, M. (2013) The response of Lake Tahoe to climate change. *Clim. Change 116*, 71–95.

6. Zhang, Y., Wu, Z., Liu, M., He, J., Shi, K., Zhou, Y., Wang, M., and Liu, X. (2015) Dissolved oxygen stratification and response to thermal structure and long-term climate change in a large and deep subtropical reservoir (Lake Qiandaohu, China). *Water Res. 75*, 249–258.

7. North, R. P., North, R. L., Livingstone, D. M., Köster, O., and Kipfer, R. (2014) Long-term

changes in hypoxia and soluble reactive phosphorus in the hypolimnion of a large temperate lake: consequences of a climate regime shift. *Glob. Change Biol. 20*, 811–823.

8. Jankowski, T., Livingstone, D. M., Bührer, H., Forster, R., and Niederhauser, P. (2006) Consequences of the 2003 European heat wave for lake temperature profiles, thermal stability, and hypolimnetic oxygen depletion: Implications for a warmer world. *Limnol. Oceanogr. 51*, 815–819.

9. Matzinger, A., Müller, B., Niederhauser, P., Schmid, M., and Wüest, A. (2010) Hypolimnetic oxygen consumption by sediment-based reduced substances in former eutrophic lakes. *Limnol. Oceanogr. 55*, 2073 – 2084.

10. Maerki, M., Müller, B., Dinkel, C., and Wehrli, B. (2009) Mineralization pathways in lake sediments with different oxygen and organic carbon supply. *Limnol. Oceanogr. 54*, 428 – 438.

11. Steinsberger, T., Schwefel, R., Wüest, A., and Müller, B. (2020) Hypolimnetic oxygen depletion rates in deep lakes: Effects of trophic state and organic matter accumulation. *Limnol. Oceanogr. 65*, 3128–3138.

12. Beutel, M. W., and Horne, A. J. (2018) Nutrient Fluxes From Profundal Sediment of Ultra-Oligotrophic Lake Tahoe, California/Nevada: Implications for Water Quality and Management in a Changing Climate. *Water Resour. Res. 54*, 1549 – 1559.

13. Burkholder, J. M. *Encyclopedia of Biodiversity*; Elsevier Inc., 2003; pp 649–670.

14. Coats, R. (2010) Climate change in the Tahoe basin: regional trends, impacts and drivers. *Clim. Change 102*, 435–466.

15. S. G. Schladow, S. W., A. Toy Tahoe: state of the lake report 2021. Available at https://tahoe.ucdavis.edu/sites/g/files/dgvnsk4286/files/inline-files/8_Physical_8.pdf (2022/12/29), 2021.

16. Ehrlich, H. L., Newman, D. K., and Kappler, A. *Ehrlich's Geomicrobiology, Sixth Edition*; CRC Press; Taylor & Francis Group: Boca Raton, 2015.

17. Nealson, K. H., and Saffarini, D. (1994) Iron and Manganese in Anaerobic Respiration: Environmental Significance, Physiology, and Regulation. *Annu. Rev. Microbiol. 48*, 311 – 343.

18. Lovley, D. R. (1991-06) Dissimilatory Fe(III) and Mn(IV) reduction. *Microbiol. Rev. 55*, 259 – 287.

19. Sorichetti, R. J., Creed, I. F., and Trick, C. G. (2014) Evidence for iron-regulated cyanobacterial predominance in oligotrophic lakes. *Freshw. Biol. 59*, 679–691.

20. Callieri, C., and Stockner, J. (2000) View of Picocyanobacteria success in oligotrophic lakes: fact or fiction? *J. Limnol. 1*, 72–76.

21. Chang, C. C. Y., Kuwabara, J. S., and Pasilis, S. P. (1992) Phosphate and Iron Limitation of Phytoplankton Biomass in Lake Tahoe. *Can. J. Fish. Aquat. Sci. 49*, 1206–1215.

22. Davison, W. (1993) Iron and manganese in lakes. *Earth-Sci. Rev. 34*, 119–163.

23. Schauser, I., Chorus, I., and Lewandowski, J. (2006) Effects of nitrate on phosphorus release: comparison of two Berlin lakes. *Acta Hydrochim. Hydrobiol. 34*, 325–332.

24. Welch, E. B., and Cooke, G. D. (2005) Internal Phosphorus Loading in Shallow Lakes: Importance and Control. *Lake Reserv. Manag. 21*, 209–217.

25. Jensen, H. S., Kristensen, P., Jeppesen, E., and Skytthe, A. (1992) Iron:phosphorus ratio in surface sediment as an indicator of phosphate release from aerobic sediments in shallow lakes. *Hydrobiol. 235-236*, 731–743.

26. Aeppli, M., Vranic, S., Kaegi, R., Kretzschmar, R., Brown, A. R., Voegelin, A., Hofstetter, T. B., and Sander, M. (2019) Decreases in Iron Oxide Reducibility during Microbial Reductive Dissolution and Transformation of Ferrihydrite. *Environ. Sci. Technol. 53*, 8736 – 8746.

27. Cutting, R. S., Coker, V. S., Fellowes, J. W., Lloyd, J. R., and Vaughan, D. J. (2009-07) Mineralogical and morphological constraints on the reduction of Fe(III) minerals by Geobacter sulfurreducens. *Geochim. Cosmochim. Acta 73*, 4004 – 4022.

28. Phillips, E. J., Lovley, D. R., and Roden, E. E. (1993-08) Composition of Non-Microbially Reducible Fe(III) in Aquatic Sediments. *Appl. Environ. Microbiol. 59*, 2727 – 2729.

29. Lovley, D. R., and Phillips, E. J. (1986-10) Availability of ferric iron for microbial reduction in bottom sediments of the freshwater tidal potomac river. *Appl. Environ. Microbiol. 52*, 751 – 757.

30. Cline, J. D. (1969) Spectrophotometric determination of hydrogen sulfide in natural waters. *Limnol. Oceanogr. 14*, 454–458.

31. Stookey, L. L. (1970) Ferrozine− a new spectrophotometric reagent for iron. *Anal. Chem. 42*, 779 – 781.

32. Lovley, D. R., and Phillips, E. J. (1987-07) Rapid assay for microbially reducible ferric iron in aquatic sediments. *Applied and Environmental Microbiology 53*, 1536 – 1540.

33. Aeppli, M., Voegelin, A., Gorski, C. A., Hofstetter, T. B., and Sander, M. (2018) Mediated Electrochemical Reduction of Iron (Oxyhydr-)Oxides under Defined Thermodynamic Boundary Conditions. *Environ. Sci. Technol. 52*, 560 – 570.

34. Gorski, C. A., Kluepfel, L. E., Voegelin, A., Sander, M., and Hofstetter, T. B. (2013) Redox Properties of Structural Fe in Clay Minerals: 3. Relationships between Smectite Redox and Structural Properties. *Environ. Sci. Technol. 47*, 13477 – 13485.

35. Kluepfel, L. E., Piepenbrock, A., Kappler, A., and Sander, M. (2014) Humic substances as fully regenerable electron acceptors in recurrently anoxic environments. *Nat. Geosci. 7*, 195 – 200.

36. Kluepfel, L. E. Redox properties and dynamics of natural organic matter as assessed by mediated electrochemical analysis. Ph.D. thesis, ETH Zurich, 2015.

37. Aeppli, M., Babey, T., Engel, M., Lacroix, E. M., Tolar, B. B., Fendorf, S., Bargar, J. R., and Boye, K. (2022) Export of Organic Carbon from Reduced Fine-Grained Zones Governs Biogeochemical Reactivity in a Simulated Aquifer. *Environmental Science & Technology 56*, 2738–2746.

38. Gorski, C. A., Kluepfel, L. E., Voegelin, A., Sander, M., and Hofstetter, T. B. (2012) Redox Properties of Structural Fe in Clay Minerals. 2. Electrochemical and Spectroscopic Characterization of Electron Transfer Irreversibility in Ferruginous Smectite, SWa-1. *Environ. Sci. Technol. 46*, 9369 – 9377.

436 39. Ravel, B., and Newville, M. (2005) ATHENA, ARTEMIS, HEPHAESTUS: data analysis for
437 X-ray absorption spectroscopy using IFEFFIT. *J. Synchrotron Radiat. 12*, 537 – 541.

438 40. Maillot, F., Morin, G., Wang, Y., Bonnin, D., Ildefonse, P., Chaneac, C., and Calas, G. (2011)
439 New insight into the structure of nanocrystalline ferrihydrite: EXAFS evidence for tetrahedrally
440 coordinated iron(III). *Geochim Cosmochim Acta 75*, 2708–2720.

441 41. Noël, V., Marchand, C., Juillot, F., Ona-Nguema, G., Viollier, E., Marakovic, G., Olivi, L.,
442 Delbes, L., Gelebart, F., and Morin, G. (2014) EXAFS analysis of iron cycling in mangrove
443 sediments downstream a lateritized ultramafic watershed (Vavouto Bay, New Caledonia).
444 *Geochim Cosmochim Acta 136*, 211–228.

445 42. Othmane, G., Allard, T., Morin, G., Sélo, M., Brest, J., Llorens, I., Chen, N., Bargar, J. R.,
446 Fayek, M., and Calas, G. (2013) Uranium Association with Iron-Bearing Phases in Mill Tailings
447 from Gunnar, Canada. *Environ Sci Technol 47*, 12695–12702.

448 43. Meyers, P. A., and Teranes, J. L. In *Tracking Environmental Change Using Lake Sediments,*
449 *Physical and Geochemical Methods*; Last, W., and Smol, J., Eds.; Developments in
450 Paleoenvironmental Research; Kluwer Academic Publishers: London, 2001; Vol. 2; pp
451 239–269.

452 44. Bray, M. S., Wu, J., Reed, B. C., Kretz, C. B., Belli, K. M., Simister, R. L., Henny, C.,
453 Stewart, F. J., DiChristina, T. J., Brandes, J. A., Fowle, D. A., Crowe, S. A., and Glass, J. B.
454 (2017) Shifting microbial communities sustain multiyear iron reduction and methanogenesis in
455 ferruginous sediment incubations. *Geobiology 15*, 678–689.

456 45. Davison, W., and Dickson, D. (1984) Mössbauer spectroscopic and chemical studies of
457 particulate iron material from a seasonally anoxic lake. *Chemical Geology 42*, 177–187.

458 46. Gadol, H. J., Elsherbini, J., and Kocar, B. D. (2022) Methanogen Productivity and Microbial
459 Community Composition Varies With Iron Oxide Mineralogy. *Frontiers in Microbiology 12*,
460 705501.

461 47. Hilton, J., Long, G., Chapman, J., and Lishman, J. (1986) Iron mineralogy in sediments. A
462 Mössbauer study. *Geochimica et Cosmochimica Acta 50*, 2147–2151.